DETERMINATION OF FILLER STRUCTURE IN SILICA-FILLED SBR COMPOUNDS BY MEANS OF SAXS AND AFM

JON OTEGUI,[1,2,*] LUIS A. MICCIO,[1,3,4] ARANTXA ARBE,[1] GUSTAVO A. SCHWARTZ,[1,3]
MATHIAS MEYER,[2] STEPHAN WESTERMANN[2]

[1]CENTRO DE FÍSICA DE MATERIALES (CSIC-UPV/EHU), P. M. DE LARDIZABAL 5, 20018 SAN SEBASTIÁN, SPAIN
[2]GOODYEAR INNOVATION CENTER LUXEMBOURG, GLOBAL MATERIALS SCIENCE, AV. GORDON SMITH, L-7750 COLMAR-BERG, LUXEMBOURG
[3]DONOSTIA INTERNATIONAL PHYSICS CENTER, P. M. DE LARDIZABAL 4, 20018 SAN SEBASTIÁN, SPAIN
[4]DEPARTAMENTO DE FÍSICA DE MATERIALES (UPV/EHU), 20080 SAN SEBASTIÁN, SPAIN

RUBBER CHEMISTRY AND TECHNOLOGY, Vol. 88, No. 4, pp. 690–710 (2015)

ABSTRACT

The structure of the silica particles network in two different solution styrene–butadiene rubbers (S-SBRs) was studied by means of small-angle X-ray scattering (SAXS) and atomic force microscopy (AFM). S-SBR compounds with different silica contents were analyzed in comparison with their oil extended counterparts. A study into the application of SAXS experiments was defined to quantify the structures of silica primary particles and clusters in filled rubber compounds up to very high levels of filler content. We propose a modified structure model that is physically more sound than the widely used Beaucage model and that leads to more robust quantification of the silica structures. In addition, an independent characterization of the filler structure was performed by means of AFM. The cluster and particle sizes deduced from both techniques are in close agreement, supporting the proposed approach. The synergetic application of SAXS and AFM allows a consistent and robust characterization of primary particles and clusters in terms of size and structure. These results were compared and discussed in the framework of previously published works. [doi:10.5254/rct.15.84893]

INTRODUCTION

Styrene–butadiene rubber (SBR) was developed in the 1930s as a replacement for natural rubber (NR) and rapidly became the most produced synthetic rubber. For automobile tires SBR rubbers are often reinforced by the addition of fillers, such as carbon black or silica particles.[1–7] In particular, activated silica reinforcement plays an important role in improving the properties of the SBR compounds.[8–11] Moreover, one of the key factors that determines the final properties of these filled compounds is commonly related to the filler structures.[12] Therefore, understanding the structure of the nanoparticles within the rubber compound becomes of utmost importance from both scientific and technological points of view. Hence, it is possible to improve both the processability of the compounds and the bulk properties of the final products.

Small-angle scattering and high-resolution microscopy techniques are very suitable for the study of filler morphologies in filled rubber compounds.[3,13–15] In particular, by combining two independent techniques such as atomic force microscopy (AFM) and small-angle X-ray scattering (SAXS), a detailed structural analysis of the silica-filled rubbers can be conducted. AFM presents the advantage of a real space analysis, but the disadvantage of a relatively small experimental two-dimensional spot size, which could restrict the representativeness of the acquired data. In comparison, SAXS data is highly representative due to the macroscopic sample size that is probed, but these data have to be fitted with a suitable model function to obtain structural information. Several structural studies in SBR and NR filled compounds have been undertaken by different groups.[16–24] However, due to the complex hierarchical morphologies associated to the fillers and their diversity of sizes, to date there is no analytical model consistently describing the structure at all length scales.

In 1995, Beaucage proposed a phenomenological model to describe hierarchical structures;[25,26] however, this model shows some limitations. To overcome some of these limitations, the

*Corresponding author. Ph: +34943018807; email: jon_otegui@ehu.es

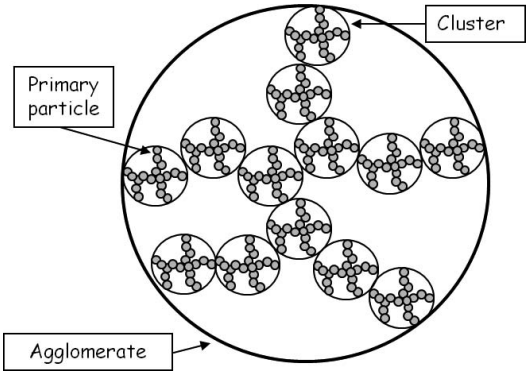

FIG. 1. — Scheme of the hierarchical structure in silica-filled SBR compounds.

present work proposes a modification of the Beaucage model that provides physically sound parameters and greater robustness of the fitting procedure. In particular, we focus our study on the structure of precipitated amorphous silica dispersed in industrial solution SBRs (S-SBRs). Finally, the structural information of the clusters and particles, independently determined by AFM and SAXS, is compared.

THEORETICAL BACKGROUND

The filler structure in rubber compounds can be described as a hierarchical structure with several characteristic length scales, as shown in Figure 1. Thus, we have primary particles; clusters of primary particles (often also called aggregates); and larger structures with clusters as basic units, namely: agglomerates.

Figure 2 shows the schematic radial averaged scattering for a filled rubber compound, that is, the scattered intensity, $I(q)$, as a function of the modulus of wave vector, q. $I(q)$ follows the power-law relationship, $I \propto q^{-d}$. The value of the exponent d is directly related to the characteristic fractal dimensions. If $d \leq 3$, the power-law exponent corresponds to the mass fractal dimension d_m, and $d = d_m$. If $3 < d < 4$, the surface fractal dimension, d_s, is related to d as follows: $d = 6 - d_s$. For a smooth surface, $d_s = 2$ but it takes a value of $d_s = 3$ for infinitely rough surfaces. In this work, we consider that

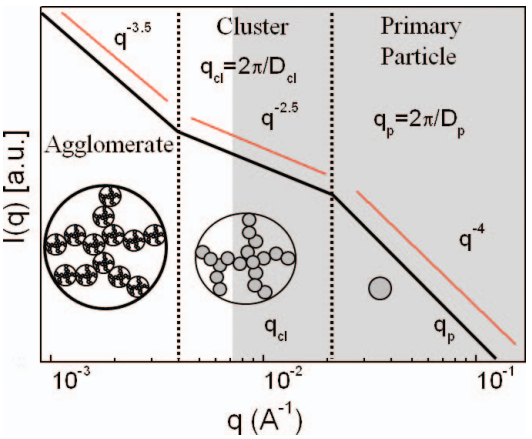

FIG. 2. — Scheme of the experimental radial averaged scattering for a typical filled rubber compound.

the primary particles are represented by spheres with a perfectly smooth surface, symbolized by $d_s = 2$.[27,28] The clusters consisting of primary particles can be described by means of a mass fractal dimension of the cluster, d_m, which corresponds to the compactness and internal structure of the cluster. In the case of a linear, rigid object, this takes a value of $d_m = 1$, whereas in the limit of infinitely compact spherical mass fractals $d_m = 3$. At this value, there is a changeover from mass fractals to surface fractals. In this work, we refer to the power law related to the primary particle as d_p and to the power law related to the cluster as d_{cl}. Therefore, as shown in Figure 2, in the q range usually covered by scattering experiments different regimens are observed. The scattering at high q values is mainly determined by the primary particles showing a scattering power law d_p close to 4. The scattering at medium q range is determined by the clusters showing a power law d_{cl}, and at lower q values an additional regime related to the agglomerates is observed. At intermediate q values, a break in the slope may be observed. The position of this break, q_p, is typically related to the average inter-particle distance D_p. In particular, q_p is approximately equal to π/R_p (radius of the primary particle) for nanoparticles in contact. In addition, another break in the slope can be found at even lower q values. In analogy to the primary particles, this second break is close to $q_{cl} = \pi/R_{cl}$ (radius of the cluster). The position of this break, q_{cl}, is typically related to the average inter-cluster distance, D_{cl}, and separates the cluster regime from the agglomerate regime. Therefore, different scaling regimes may be observed in the scattering diagram. The transition between the different slopes of $d_p \approx 4$ ($d_s = 2$) to $d_{cl} = d_m \approx 2.5$ identifies the involved characteristic sizes.[29] In this context, the measured scattering from the nanocomposites arises from the primary particles and the superstructures they are forming: clusters and agglomerates. Conventional laboratory SAXS measurements cover the q range related to the primary particle and cluster regimes, as shown by the gray area in Figure 2.

UNIFIED BEAUCAGE MODEL

One of the most used approaches for the evaluation of the characteristic clusters and particles sizes is the unified model of Beaucage. This model has often been applied for the characterization of the multi-level structure of particles in different systems.[25,26] In the framework of the Beaucage model the scattering of the system is given by

$$I(q) \cong I_{cl}(q) + I_p(q) \tag{1}$$

where $I_{cl}(q)$ is the scattering contribution from the clusters,

$$I_{cl}(q) \cong H_1 \exp\left(\frac{-q^2 \overline{R_{g,cl}^2}}{3}\right) + H_2 \exp\left(\frac{-q^2 \overline{R_{g,p}^2}}{3}\right) \times \left[\left\langle \frac{\left(erf(q\,\overline{R_{g,cl}}/\sqrt{6})\right)^3}{\overline{R_{g,cl}^2} q} \right\rangle\right]^{d_{cl}} \tag{2}$$

and $I_p(q)$ is the contribution from the primary particles,

$$I_p(q) \cong H_3 \exp\left(\frac{-q^2 \overline{R_{g,p}^2}}{3}\right) + H_4 \left[\frac{\left(erf(q\,\overline{R_{g,p}}/\sqrt{6})\right)^3}{\overline{R_{g,p}} q}\right]^{d_p} \tag{3}$$

Here, the scattering of the primary particles and the clusters is assumed to be independent from each other, allowing an incoherent sum of both contributions. In addition, each contribution is given by an additive combination of a Guinier law and a term accounting for the scattering in the Porod regime. The fitting parameters of this model are the average radius of gyration of the primary particles, $\overline{R_{g,p}}$; its fractal surface dimension of the primary particles, d_p; the average cluster radius of gyration, $\overline{R_{g,cl}}$; and its mass fractal dimension, d_{cl}. In addition, the four pre-factors H_{1-4} are also

free fitting parameters. As introduced here, these pre-factors have no distinct physical meaning; however, the relationship $H_1 = N_{p,B} H_3$ is often used in the literature, which serves for the estimation of the average number of particles per cluster, $N_{p,B}$.[17] In total, the Beaucage model has eight fitting parameters. Therefore, one of the goals of the present work is to propose a new model based on recent developments of the Beaucage model to reduce the number of parameters and to establish a consistent dependence among them. This modified Beaucage model (MBM) will help provide a better understanding of the complex hierarchical morphology of the fillers.

MODIFICATION OF THE BEAUCAGE MODEL

In this section, we extend the unified Beaucage model to correlate its free parameters with physical observables characterizing the particle system.[30] First, for dilute non-interacting single particles, the scattering in the Guinier regime, that is, at $qR_{g,p} < 1$ can be described by the Guinier function:

$$I(q) \cong G_p \exp\left(\frac{-q^2 \langle R_{g,p}^2 \rangle}{3}\right) \tag{4}$$

Compared to Eq. 3, we include the polydispersity of the system explicitly. The average radius of gyration is given by the relation between the eighth and sixth momentum of the particle radius:

$$\langle R_{g,p}^2 \rangle = \frac{3}{5} \frac{\langle R_p^8 \rangle}{\langle R_p^6 \rangle} \tag{5}$$

In addition, from now on the corresponding pre-factors H_x will be referred as G_p, B_p, G_{cl}, and B_{cl} to stress the fact that in the MBM they are no longer independent from each other. By comparing this function with the analytical exact form factor for polydisperse spheres with log-normal distributed sizes, one obtains the following:

$$G_p = \varphi_p \Delta\rho^2 \frac{\langle V_p^2 \rangle}{\langle V_p \rangle} \tag{6}$$

Here, φ_p denotes the volume fraction of the particle, $\langle V_p \rangle = \frac{4\pi}{3} \langle R_p^3 \rangle$ and $\langle V_p^2 \rangle = \left(\frac{4\pi}{3}\right)^2 \langle R_p^6 \rangle$ the first and second moment of the average particle volume; and $\Delta\rho^2 = (\rho_p - \rho_0)^2$ denotes the contrast given by the difference in the scattering length density between the particles and the surrounding medium, that is, the polymer and the other additives. From the definition of the lognormal distribution,

$$f(r) = \frac{1}{r\sigma\sqrt{2\pi}} \exp\left(\frac{\ln(r/R_{av})}{2\sigma^2}\right) \tag{7}$$

the n-th moment of the average radius is as follows:

$$\langle R^n \rangle = R_{av}^n \exp\left(\frac{n^2\sigma^2}{2}\right) \tag{8}$$

Furthermore, assuming a smooth surface of the primary particle ($d_p = 4$, $d_s = 2$), the scattering at high q values, that is, in the so-called Porod regime, is determined by

$$I(q \to \infty) \cong \frac{8\pi^2 \varphi_{Si} \Delta\rho^2 \langle S_p \rangle}{\langle V_p \rangle} q^{-4} \tag{9}$$

Here, $\langle S_p \rangle$ is the average surface (proportional to the second moment of the lognormal distribution). By comparison with the leading term of the Beaucage function at high q, we can

derive the following:

$$B_p = 6\pi\ \varphi_{\ p}\Delta\rho^2 \frac{\langle R_p^2\rangle}{\langle R_p^3\rangle} \tag{10}$$

Combining this information, the form factor of polydisperse particles can be described by the following:

$$P_p(q) \cong G_p \exp\left(\frac{-q^2\langle R_{g,p}^2\rangle}{3}\right) + B_p\left[\frac{\left(erf\left(\sqrt{q^2\langle R_{g,p}^2\rangle/6}\right)\right)^3}{q}\right]^{d_p} \tag{11}$$

As a last step we include a particle interaction by a virial expansion, as introduced first by Zimm:[31]

$$I(q) \cong \frac{1}{\frac{1}{P_p(q)} + A_2} \tag{12}$$

Although this shows an extremely rough approximation for as high particle volume fraction as we have, this ansatz can be nevertheless used, since the scattering in the affected q regime is dominated by the scattering from the superstructures of the primary particles, that is, the clusters, and this expansion phenomenologically accounts for the reduction of the scattered signal due to the correlation holes arising from the inter-particle correlation within the mentioned clusters.

Next, we extend the model to a second level, a level that includes the contributions from the aggregated particles, the previously mentioned clusters. In analogy to the primary particles, the scattering contribution at $qR_{g,\,cl} < 1$ is again dominated by the Guinier term:

$$I(qR_{g,cl}<1) \cong \varphi_p\Delta\rho^2 \frac{\langle V_p^2\rangle}{\langle V_p\rangle}\overline{N_{p,MBM}} \exp\left(\frac{-q^2\overline{R_{g,cl}^2}}{3}\right) \tag{13}$$

This expression differs from Eq. 4 only by a pre-factor $\overline{N_{p,MBM}}$, a measure for the average number of particles per cluster, and, of course, the radius of gyration of the particles is replaced by the radius of gyration of the clusters. As in the Beucauge model, $\overline{R_{g,cl}}$ represents the average cluster radius of gyration. The derivation of the pre-factor in the Porod term of the Beaucage model for the clusters is more complicated. However, with the corrections of Hammouda[32] for the pre-factor, one can find the following:

$$B_{cl} = \frac{\varphi_p\Delta\rho^2 d_{cl}\langle V_p\rangle}{\left(\overline{R_{g,cl}}\right)^{d_{cl}}}\left(\frac{6d_{cl}^2}{(2+d_{cl})(2+2d_{cl})}\right)\overline{N_{p,MBM}} \tag{14}$$

Therefore, the scattering contribution from the cluster is accounted via

$$I_{cl}(q) \cong G_{cl}\exp\left(\frac{-q^2\overline{R_{g,cl}^2}}{3}\right) + B_{cl}\exp\left(\frac{-q^2\langle R_{g,p}^2\rangle}{3}\right)\left[\frac{\left(erf\left(\sqrt{q^2\overline{R_{g,cl}^2}/6}\right)\right)^3}{q}\right]^{d_{cl}} \tag{15}$$

Here, the additional exponential expression takes the vanishing contributions from the clusters below $qR_{g,\,p} > 1$ into account. To summarize, the total scattering in the observed q regime can be approximated by the modified Beaucage model that has seven fitting parameters:

$$I(q) \cong I_{cl}(q) + \frac{1}{\frac{1}{P_p(q)} + A_2} \tag{16}$$

In addition to the reduction of free fitting parameters, the presented modified Beaucage model has further advantages. First, we introduced an additional term to account for the inter-particle correlations; this additional term especially improves the fitting in the cross-over region. Moreover, the number of particles per cluster can be determined more precisely due to the clear separation of both contributions, from the particles and clusters (this point is further discussed in the rationalization of the results). Second, the structure of the original Beaucage model is such that there are four terms that can contribute to the scattering intensity in a somewhat arbitrary way, controlled by the parameters H_x. A physical interpretation is done only after the actual fitting, where some system characteristics are derived from their adjusted values and may lead to unphysical combinations of H_x. In contrast, the proposed modified model described herein intrinsically introduces the physical dependencies and leads to a coupling of the four terms. Thereby, unphysical fit results are hindered and a more stable fitting process is obtained.

EXPERIMENTAL ANALYSIS

MATERIALS

Two different S-SBRs, labeled S-SBR and S-SBR-o were studied in this work. S-SBR composition (in weight percent) is 25% styrene, 50% 1–2 vinyl, 15.4% 1–4 trans, and 9.6% 1–4 cis co-monomer distribution. In contrast, S-SBR-o is a random copolymer with 25% styrene, 47% 1–2 vinyl, 17.0% 1–4 trans, and 11.0% 1–4 cis. The S-SBR-o was pre-mixed with 37.55 per hundred rubber, parts in weight per 100 parts of rubber (phr) of extender-treated distillate aromatic extracts (TDAE oil). Amorphous silica (Z1165 MP-Rhodia) with a specific surface area (S_{sp}) of 165.8 m^2/g was used as filler. Samples with five different volume fractions, 0, 15, 30, 70, and 90 phr, were prepared using bis-3-triethoxysilylpropyldisulfide as coupling agent. The sample labels show the filler content and the oil and non-oil extension, respectively. A detailed sample composition is shown in Table I, where the antioxidant is *N*-(1,3)-dimethylbutyl-*N*′-phenyl-p-phenylenediamine, the accelerator is *N*-cyclohexyl-2-benzothiazolesulfeneamide, and the secondary accelerator is diphenylguanidine. The mixing process of rubber, filler, and additives was performed in an intermeshing mixer (internal volume 3.6 liters) with constant fill factor in three stages: two dispersion stages and one productive stage. In both non-productive stages the mixing time for all compounds was set to 2 min after reaching 160 °C. For all the compounds 15 cm ×15 cm square sheet samples (thickness of ~0.7 mm) were obtained by compression-molding vulcanization (170 °C for 10 min).

SAXS SETUP

The SAXS experiments were conducted on a three-pinhole PSAXS-L instrument (Rigaku, Auburn Hills, MI, USA) operating at 45 kV and 0.88 mA. The MicroMax-002 X-ray generator system (Rigaku) is composed by a microfocus sealed tube source module and an integrated X-ray generator unit that produces CuKα transition photons of wavelength $\lambda = 1.54$ nm. The flight path and the sample chamber in this equipment are under vacuum. The scattered X-rays are detected on a two-dimensional multi-wire X-ray detector (Gabriel design, 2D-200X; Rigaku). This gas-filled proportional type detector offers a 200 mm diameter active area with approximately 200 μm resolution. The azimuthally averaged scattered intensities were obtained as a function of momentum transfer $q = (4\pi/\lambda)/\sin\theta$, where θ is half the scattering angle. Reciprocal space calibration was done

TABLE I
COMPOSITION OF S-SBR/S-SBR-o SAMPLES[a]

	Unfilled		15 phr		30 phr		50 phr		70 phr		90 phr	
Rubber (S-SBR/S-SBR-o)	100	137.5	100	137.5	100	137.5	100	137.5	100	137.5	100	137.5
Filler	—	—	15	15	30	30	50	50	70	70	90	90
Coupling agent	—	—	1.2	1.2	2.4	2.4	4	4	5.6	5.6	7.2	7.2
Antioxidant	0.75	0.75	0.75	0.75	0.75	0.75	0.75	0.75	0.75	0.75	0.75	0.75
Stearic acid	3	3	3	3	3	3	3	3	3	3	3	3
TDAE oil	15	*	15	*	15	*	15	*	15	*	15	*
Antioxidant 2	1.75	1.75	1.75	1.75	1.75	1.75	1.75	1.75	1.75	1.75	1.75	1.75
Zinc oxide	2.5	2.5	2.5	2.5	2.5	2.5	2.5	2.5	2.5	2.5	2.5	2.5
Accelerator	2.3	2.3	2.3	2.3	2.3	2.3	2.3	2.3	2.3	2.3	2.3	2.3
Sulfur	1.5	1.5	1.5	1.5	1.5	1.5	1.5	1.5	1.5	1.5	1.5	1.5
Secondary accelerator	—	—	0.75	0.75	1	1	1.3	1.3	1.7	1.7	2	2

[a] All quantities are given in parts in weight per 100 parts of rubber.

using silver behenate as standard. Measurements were performed at room temperature with a sample to detector distance of 2 m. The data were background corrected by subtracting the result of a measurement on the unfilled sample applying the proper transmission corrections.

AFM SETUP

Silica-filled SBR samples of 200 μm thickness (nominal) were obtained using a microtome. The filler structures were characterized by using a Multimode 8 atomic force microscope (Bruker, Billerica, MA, USA). Moderate/hard ($A_{sp}/A_0 = 0.6/0.5$, where A_{sp} is the set point amplitude and A_0 is the free oscillation amplitude) or soft ($A_{sp}/A_0 = 0.1$) tapping images in air were obtained by using RTESP7 or HMX-10 probes (Bruker). Nominal values (manufacturer) for the natural frequency, tip radius, and cantilever spring constant of RTESP7 probes are $f_0 = 250$–336 kHz, $R = 8$ nm, and $k =$ 20–80 N/m, respectively. A mechanical characterization of the materials at the nanoscale was performed by using HarmoniX AFM imaging.[33–35] HarmoniX can provide simultaneous information about various mechanical aspects of the sample, such as peak force, modulus, and surface adhesion, to name a few. For these measurements, specifically designed torsional harmonic cantilevers were used (previously mentioned HMX-10). The nominal values (manufacturer) for the natural frequency, tip radius, and cantilever spring constant for these probes are $f_0 = 70$ kHz, $R = 10$ nm, and $k = 1.5$–6 N/m, respectively. The acquired images were processed by using WSxM software.[36]

AFM ANALYSIS OF SILICA STRUCTURES IN SILICA-FILLED COMPOUNDS

Figure 3 shows AFM topography and phase images (soft tapping) of typical filler structures observed in several areas of S-SBR samples. Although there is a clear correlation between the presence of silica clusters and topographic features, no detailed information about the cluster structure can be obtained through this channel. The mechanical phase, in contrast, does provide a very good contrast between silica and rubber, which in turn allows a precise detection of the different structures. There is a rather homogeneous filler distribution along the rubber matrix, independently of the formulation (Figure 3b, h). Typical clusters can be observed in more detail at higher zoom levels (Figure 3f, l). At first sight, there are no remarkable differences between clusters in S-SBR or in S-SBR-o compounds. A detailed statistical analysis is performed in Appendix.

RESULTS AND DISCUSSION

AFM

Table 2 summarizes the cluster size obtained by means of AFM experiments. In this case, $\langle R_i \rangle$ stands for the apparent radius obtained directly from the AFM images. Alternatively, $\langle R \rangle$ stands for the corrected radius obtained by taking into account the cutting effect and the method limitations, whereas σ and $\langle R_{cl}^{AFM} \rangle$ represent the standard deviation and the average radius obtained from the lognormal distribution (according to the first moment of Eq. 8). For a detailed discussion of the statistical analysis, see Appendix.

As shown, $\langle R_i \rangle$ decreases with increasing silica volume fraction for both formulations; simultaneously, a systematic increment of σ is observed. Therefore, $\langle R_{cl}^{AFM} \rangle$ decreases monotonically with increasing silica content. Figure 4 shows $\langle R_{cl}^{AFM} \rangle$ as a function of silica volume fraction, where this tendency can be easily observed. Recent work shows that this tendency can be related to the mixing procedure.[17,22] As silica content increases, typical cluster distances decrease, in turn increasing compound viscosity and therefore shear forces, breaking up the aggregates into smaller pieces. Within error bars, cluster sizes are nearly the same for both formulations along the analyzed concentration range.

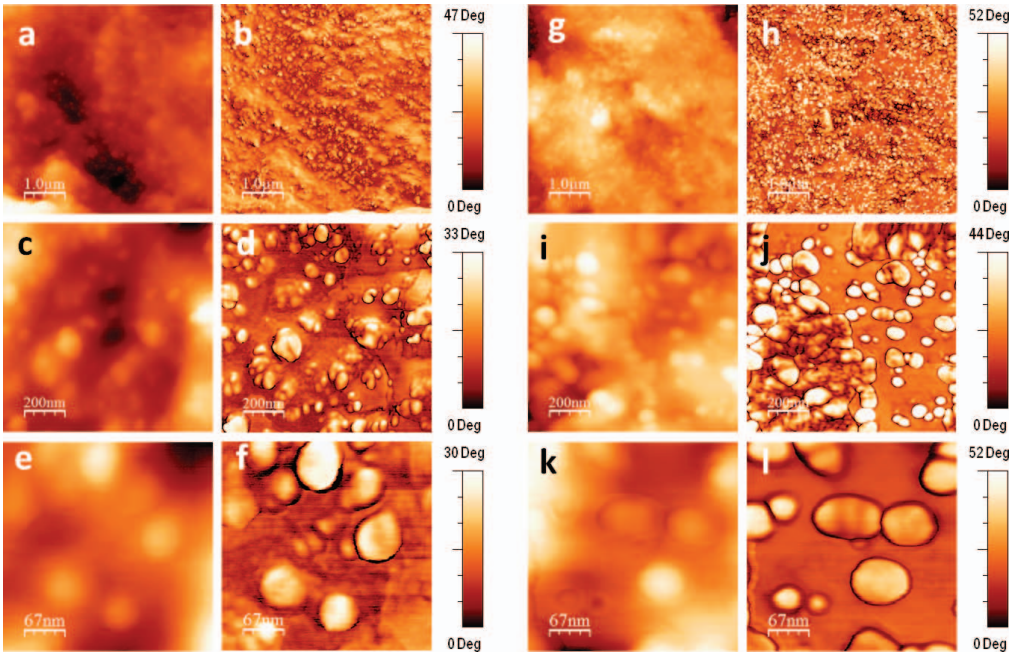

FIG. 3. — Typical filler structures of S-SBR and S-SBR-o with 50 phr observed by soft tapping acquired at different zoom levels (topography and phase images, respectively). S-SBR-o: (a and b) 5 μm; (c and d) 1 μm; (e and f) 330 nm. S-SBR: (g and h) 5 μm; (i and j) 1 μm; (k and l) 330 nm.

SAXS

Beaucage Analysis. In a first step to extract constitutive parameters, the scattering diagrams were fitted by the unified model of Beaucage described in Theoretical Background. As shown in Figure 5, the fitted model follows closely the scattering experimental results.

According to the specific surface area, $S_{sp} = 165.8$ m^2/g, the radius of the particle can be calculated from the relation $\overline{R_p} = 3/(S_{sp}\rho) = 11.1$ nm, assuming $\rho = 2$ g/cm^3 for the density of the silica particles. Considering these particles as homogeneous spheres, the radius $\overline{R_p}$ can be related with the radius of gyration $\overline{R_{g,p}}$ through $R^2 = 5/3R_g{}^2$. As the fittings with the Beaucage model are not stable when using $\overline{R_{g,p}}$ as a free parameter, taking into account the previous assumptions, the radius of gyration of the primary particle was fixed to $\overline{R_{g,p}} = 8.6$ nm.

In addition, the value of $\overline{R_{g,cl}}$ was obtained as a free parameter from the corresponding fitting. A general expression to estimate $\overline{R_{cl}}$ from $\overline{R_{g,cl}}$ is written below (assuming the clusters as spherically isotropic mass fractal structures[37]),

TABLE II
AFM SIZE DISTRIBUTION RESULTS

S-SBR/S-SBR-o, phr	$\langle R_i \rangle$, nm		σ		$\langle R \rangle$, nm		$\langle R_{cl}^{AFM} \rangle$, nm	
15	36	37	0.36	0.22	46	47	49	48
30	30	30	0.4	0.42	38	38	41	42
50	25	28	0.44	0.35	32	36	35	38
70	21	24	0.48	0.51	27	31	30	35

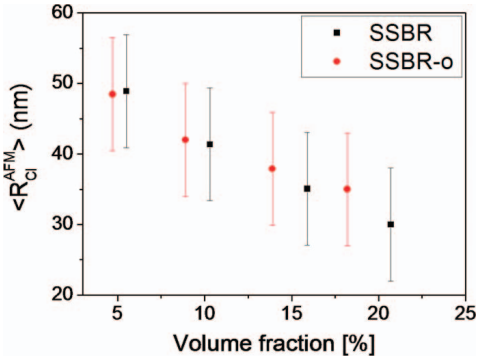

FIG. 4. — $\langle R_{Cl}^{AFM} \rangle$ as a function of the silica content (volume fraction) obtained through AFM measurements.

$$\overline{R_{cl}^2} = \left(\frac{d_{cl}+2}{d_{cl}}\right)\overline{R_{g,cl}^2} \tag{17}$$

where d_{cl} is the corresponding mass fractal dimension of the cluster. As we mentioned in Theoretical Background, if infinitely compact spherical mass fractals are considered, then $d_{cl}=3$ and a particularization of this equation is obtained ($\overline{R_{cl}^2} = 5/3\ \overline{R_{g,cl}^2}$). $\overline{R_{cl}}$ calculated from the Eq. 17 is presented in Table 4. For the S-SBR compounds the values for $\overline{R_{cl}}$ range from 23.2 up to 30.5 nm.

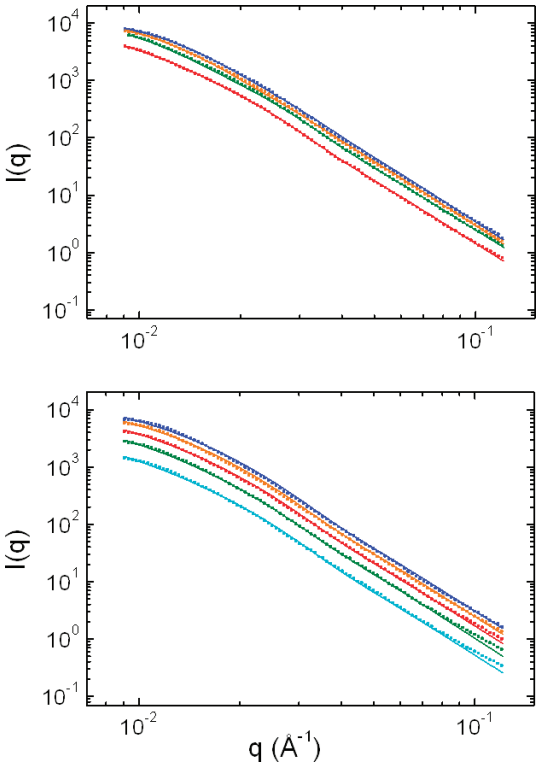

FIG. 5. — Scattering data and the corresponding Beaucage fitting for S-SBR (above) and S-SBR-o (below) compounds. Dots stand for the experimental results, and solid lines stand for fittings: light blue, 15 phr; red, 30 phr; green, 50 phr; orange, 70 phr; dark blue, 90 phr.

TABLE III
STRUCTURAL PARAMETERS FITTED WITH BEAUCAGE MODEL FOR X-RAY MEASUREMENTS ON SILICA-FILLED SAMPLES

		Fixed parameter		Fitting parameter					
Sample	Φ, vol%	$\overline{R_{g,p}}$, nm	d_p	H_1	H_2	H_3	H_4	$\overline{R_{g,cl}}$, nm	d_{cl}
S-SBR 30 phr	10.3	8.6	4	11 163	26 136	820	4964	22.3	2.4
S-SBR 50 phr	15.9	8.6	4	16 222	24 560	1535	7641	20.8	2.4
S-SBR 70 phr	20.7	8.6	4	14 527	14 189	1900	12 578	18.1	2.3
S-SBR 90 phr	24.9	8.6	4	13 431	7898	2507	14 269	17.0	2.3
S-SBR-o 15 phr	4.7	8.6	4	917	3268	32	169	39.7	2.3
S-SBR-o 30 phr	8.9	8.6	4	1414	5962	55	396	37.6	2.3
S-SBR-o 50 phr	13.9	8.6	4	1944	7828	93	554	35.3	2.3
S-SBR-o 70 phr	18.2	8.6	4	2157	10 264	133	802	33.0	2.3
S-SBR-o 90 phr	22.0	8.6	4	2563	11 144	170	119	31.6	2.3

However, fitting of the oil extended materials yielded much larger values, ranging from 43.2 to 54.3 nm. Concerning the cluster description, the fit provides a mass fractal dimension, d_{cl}, that is independent of filler concentration. All of these results are summarized in Tables 3 and Table 4.

Although the statistic description of the experimental curves is rather good, the obtained results do not agree with those observed by using AFM. In particular, S-SBR-o cluster sizes are apparently overestimated by the Beaucage model. Moreover, the aggregation numbers, calculated as $N_{p,B} = H_1/H_3$ and shown in Table 4, are lower in comparison with the literature-reported values for similar systems.[17,22,23] The main reason could be related to the fact that the pre-factors $H_{1–4}$ are not correlated among each other. However, from scattering theory, they should be intrinsically correlated to have a physical meaning. In the MBM, we use these dependencies to stabilize the fitting (see Theoretical Background).

MBM Analysis. Figure 6 displays the experimental SAXS scattering diagrams of silica-filled styrene butadiene rubbers and the corresponding fits with the MBM. To obtain physical values of the cluster size from the MBM fitting, we constrained the possible high and low $\overline{R_{cl}}$ limits: a) the average inter-particle distance of 20 nm, obtained from D_p values ranging from 18.5 to 22 nm ($D_p = 2\pi/q_p$), is considered as the low cluster size limit (where q_p is obtained from the break in the

TABLE IV
CALCULATED QUANTITIES FROM FITTED BEAUCAGE MODEL PARAMETERS

Sample	Φ, vol%	$\overline{R_{cl}}$, nm	$N_{p,B} = H_1/H_3$	$N_{p,R_g} = \left(\frac{\overline{R_{g,cl}}}{\overline{R_{g,p}}}\right)^{d_{cl}}$
S-SBR 30 phr	10.3	30.5	13.4	11.0
S-SBR 50 phr	15.9	28.4	10.4	9.3
S-SBR 70 phr	20.7	24.7	7.6	6.7
S-SBR 90 phr	24.9	23.2	5.4	4.3
S-SBR-o 15 phr	4.7	54.3	28.6	29.6
S-SBR-o 30 phr	8.9	51.4	25.7	26.1
S-SBR-o 50 phr	13.9	48.3	20.9	22.6
S-SBR-o 70 phr	18.2	45.1	16.2	19.3
S-SBR-o 90 phr	22.0	43.2	15.0	17.5

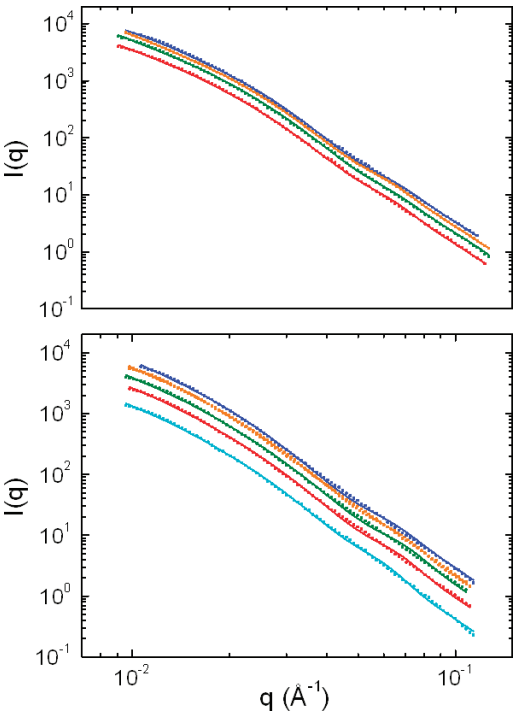

FIG. 6. — Scattering data and MBM fitting for S-SBR (above) and S-SBR-o (below) compounds. Dots stand for the experimental results, and solid lines stand for fittings: light blue, 15 phr; red, 30 phr; green, 50 phr; orange, 70 phr; dark blue, 90 phr.

scattering diagram slope, as explained in Theoretical Background) and b) a rough estimation of the upper $\overline{R_{cl}}$ fitting constraint ($\overline{R_{cl}} = 100$ nm) was performed from independent Krakty plots (data not shown). The obtained fitting parameters, specifying the nature and architecture of the filler, are summarized in Table 5 for all investigated samples. The fitting with MBM is more stable than that with the unified Beaucage model. This is because the Beaucage model allows several combinations of the H_1, H_2, H_3, and H_4 values to describe the experimental curves, whereas the corresponding parameters are physically coupled.

As mentioned above, we assume a lognormal distribution of the primary particles size (Eq. 7), described by R_{av} and σ.[38] In this context, the average radius of the primary particle $\langle R_p \rangle$ is given by Eq. 8. Within error bars, the average primary particle radius $\langle R_p \rangle$ is constant for all studied compounds (see Figure 7 and Table 6); therefore, an average radius across all compounds of $\langle \overline{R_p} \rangle = 6.63 \pm 0.18$ nm can be calculated. Concerning the cluster description, the fit provides the cluster radius of gyration, $\overline{R_{g,cl}}$; the mass fractal dimension of the cluster, d_{cl}; and the number of particles per cluster or aggregation number, $\overline{N_{p,MBM}}$ (Table 5).

As explained above, we consider the clusters as spherically isotropic fractal structures. Therefore, the radius of the cluster, $\overline{R_{cl}}$, can be determined according to Eq. 17. As depicted in Figure 7 (see also Table 6), the obtained $\overline{R_{cl}}$ decreases as the filler fraction increases. In addition, for a given rubber type, d_{cl} does not change with the filler concentration. However, systematic differences ($\sim$10%) can be observed for S-SBR and S-SBR-o. Although an average value of 2.3 is obtained for S-SBR compounds, S-SBR-o compounds show a value of $\sim$2.4. As explained in Theoretical Background, d_{cl} is related with the fractal distribution of the primary particle inside the

TABLE V
STRUCTURAL PARAMETERS FITTED WITH MBM APPROACH FOR X-RAY MEASUREMENTS ON SILICA-FILLED SAMPLES

	Fixed		Fitting parameters					
Sample	Φ_{Si}, vol%	d_p	$R_{p,av}$, nm	σ	A_2	$\overline{R_{g,cl}}$, nm	d_{cl}	$\overline{N_{p,MBM}}$
S-SBR 30 phr	10.3	4	6.90 ± 0.39	0.103 ± 0.004	0.075 ± 0.007	33.2 ± 3.2	2.28 ± 0.05	32.5 ± 5.0
S-SBR 50 phr	15.9	4	6.54 ± 0.47	0.122 ± 0.005	0.061 ± 0.009	29.9 ± 3.6	2.26 ± 0.05	28.2 ± 6.6
S-SBR 70 phr	20.7	4	6.73 ± 0.58	0.119 ± 0.005	0.038 ± 0.014	24.8 ± 3.0	2.32 ± 0.05	17.0 ± 4.4
S-SBR 90 phr	24.9	4	6.63 ± 0.54	0.108 ± 0.007	0.042 ± 0.011	21.0 ± 3.9	2.31 ± 0.05	12.0 ± 5.5
S-SBR-o 15 phr	4.7	4	6.39 ± 0.61	0.171 ± 0.007	0.135 ± 0.031	39.8 ± 5.9	2.31 ± 0.07	45.5 ± 4.4
S-SBR-o 30 phr	8.9	4	6.78 ± 0.78	0.092 ± 0.009	0.010 ± 0.006	36.6 ± 4.3	2.42 ± 0.09	38.9 ± 7.1
S-SBR-o 50 phr	13.9	4	6.39 ± 0.63	0.103 ± 0.013	0.097 ± 0.011	32.4 ± 4.8	2.43 ± 0.08	35.1 ± 8.1
S-SBR-o 70 phr	18.2	4	6.52 ± 0.75	0.100 ± 0.012	0.062 ± 0.008	29.9 ± 5.1	2.42 ± 0.09	31.0 ± 8.9
S-SBR-o 90 phr	22.0	4	6.77 ± 0.85	0.102 ± 0.014	0.044 ± 0.009	27.7 ± 4.3	2.40 ± 0.08	25.4 ± 7.5

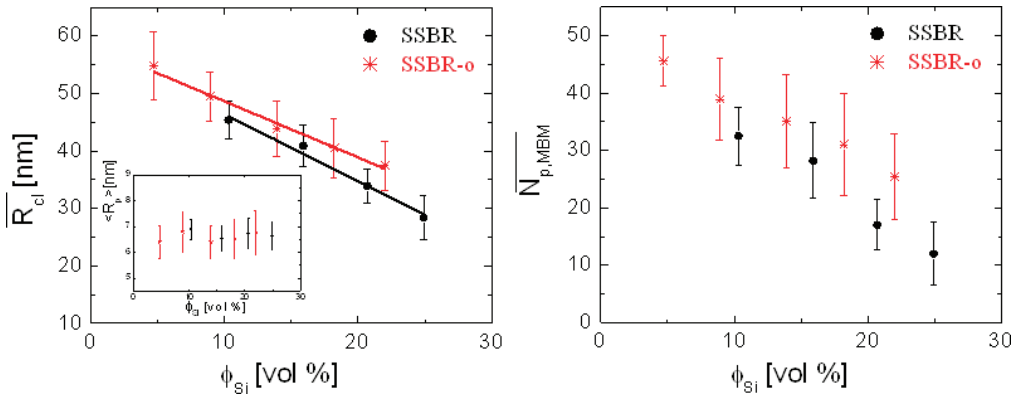

FIG. 7. — (a) $\overline{R_{cl}}$ as a function of silica content for S-SBR and S-SBR-o compounds. Inset shows $\langle R_p \rangle$ as a function of silica content. (b) $\overline{N_{p,MBM}}$ as a function of silica content.

clusters, that is, with the cluster compactness. According to the d_{cl} definition, the MBM reveals more compact silica clusters in the oil extended compounds.

The aggregation number is obtained from MBM fitting ($\overline{N_{p,MBM}}$) as well. Figure 7b shows the results for S-SBR and S-SBR-o compounds as a function of silica volume fraction. In particular, the differences between compounds are more pronounced in the $\overline{N_{p,MBM}}$ representation. An alternative way to calculate the aggregation number, depending on R_{cl} and d_{cl}, can be found in the literature:[30]

$$N_{p,R_g} = \left(\frac{\overline{R_{g,cl}}}{R_{g,p}} \right)^{d_{cl}} \tag{18}$$

Specifically, Eq. 18 shows that a higher $N_{p,Rg}$ value in S-SBR-o is related to a higher compactness as well as to a higher $\overline{R_{g,cl}}$. Therefore, the combination of a slightly higher $\overline{R_{g,cl}}$ and a higher d_{cl} for S-SBR-o compounds explains the differences compared to S-SBRs. In this context, the results of $N_{p,Rg}$ (Table 6) are in good agreement with the $\overline{N_{p,MBM}}$ values obtained from the MBM fittings for S-SBRs, but they are higher for S-SBR-o compounds.

TABLE VI
CALCULATED QUANTITIES FROM FITTED MBM PARAMETERS

Sample	Φ_{Si}, vol%	R_p, nm	$\overline{R_{cl}}$, nm	$N_{p,R_g} = \left(\frac{\overline{R_{g,cl}}}{R_{g,p}} \right)^{d_{cl}}$
S-SBR 30 phr	10.3	6.93	45.4	35.6
S-SBR 50 phr	15.9	6.60	40.9	30.4
S-SBR 70 phr	20.7	6.77	33.9	20.3
S-SBR 90 phr	24.9	6.67	28.4	11.1
S-SBR-o 15 phr	4.7	6.48	54.9	66.2
S-SBR-o 30 phr	8.9	6.81	49.5	58.5
S-SBR-o 50 phr	13.9	6.43	43.9	50.9
S-SBR-o 70 phr	18.2	6.55	40.5	39.4
S-SBR-o 90 phr	22.0	6.81	37.5	29.0

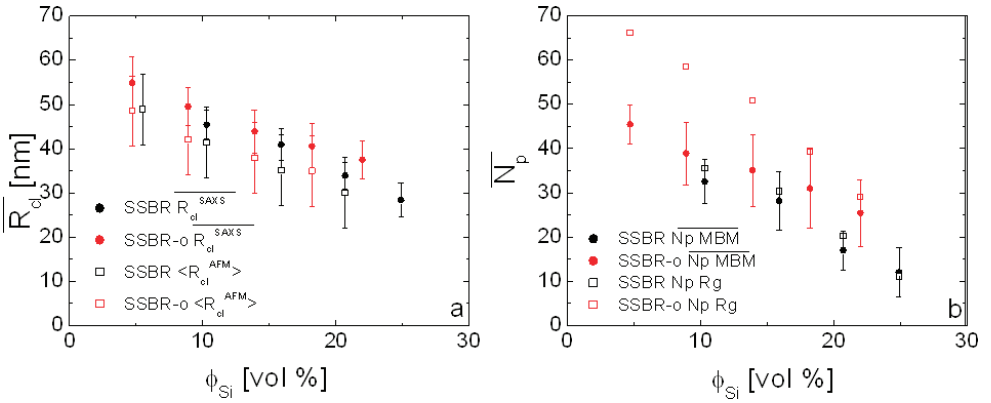

FIG. 8. — MBM and AFM analysis results: (a) $\overline{R_{cl}^{SAXS}}$ and $\langle R_{cl}^{AFM} \rangle$; (b) $\overline{N_{p,MBM}}$ and $N_{p,Rg}$.

RATIONALIZATION OF RESULTS

In this work, the silica structure in the rubber compounds has been studied by using two independent approaches, AFM and SAXS. It is shown that, despite their limitations, the combination of these complementary techniques can be used in a synergetic manner to establish a robust characterization of silica structures in rubber compounds.

Structural Filler Information by SAXS and AFM. As shown in the previous sections, the primary particle size distribution does not depend on the silica content or rubber formulation. The frictional forces that come out during the mixing stage are not able to break them. Moreover, the observed radii are slightly smaller than reported values for similar systems. This difference could be related with the origin of these values; the radius of the primary particle is commonly obtained from the corresponding density and specific surface area $\overline{R_p} = 3/(S_{sp}\rho)$.[19] However, the so-calculated average radius is proportional to the ratio third/second moment of $\langle R_p^n \rangle$, leading to an overestimation of $\overline{R_p}$. On the contrary, in this work $\langle R_p \rangle$ is directly retrieved from the lognormal distribution parameters (R_{av} and σ) obtained from the MBM fitting. Another important point to be addressed is the fractal dimension of the particles. As shown in Unified Beaucage Model, one of the MBM assumptions is that $d_p = 4$ ($d_s = 2$, corresponding to a perfectly smooth particle). The agreement between the fittings and the scattering data further support the validity of this assumption.

In the case of the clusters, it is observed that $\overline{R_{cl}^{SAXS}}$ and $\langle R_{cl}^{AFM} \rangle$ decrease as the silica content increases. A possible reason might be the increase of the frictional forces among clusters during the mixing process when increasing the silica content. As silica content increases, the cluster distance decreases (i.e., the clusters interaction increases), in turn increasing the frictional force among clusters and the corresponding breaking process. It is necessary to stress that the mixing time was kept constant to remove the influence of the mixing procedure. Furthermore, the cluster sizes resulting from SAXS analysis (see Figure 8a) show systematically bigger radii for S-SBR-o compounds compared to their S-SBR counterparts. Higher oil concentrations could be related to lower shear stresses and therefore higher cluster sizes. In addition, MBM shows a 10% higher S-SBR-o fractal dimension of the clusters. Accordingly, it can be concluded that the S-SBR-o compounds studied here show more compact clusters than S-SBRs. The same $\overline{R_{cl}^{SAXS}}$ trend is followed by the aggregation number of the compounds, which depend on $\overline{R_{g,cl}}$ and d_{cl}. This tendency agrees well with literature results for similar SBR silica systems as discussed in the section below. In addition, a noticeable difference in $\overline{N_p}$ has been obtained between S-SBR and S-SBR-o compounds (see Figure 8b). It is found that this value, obtained by using two different methods, is

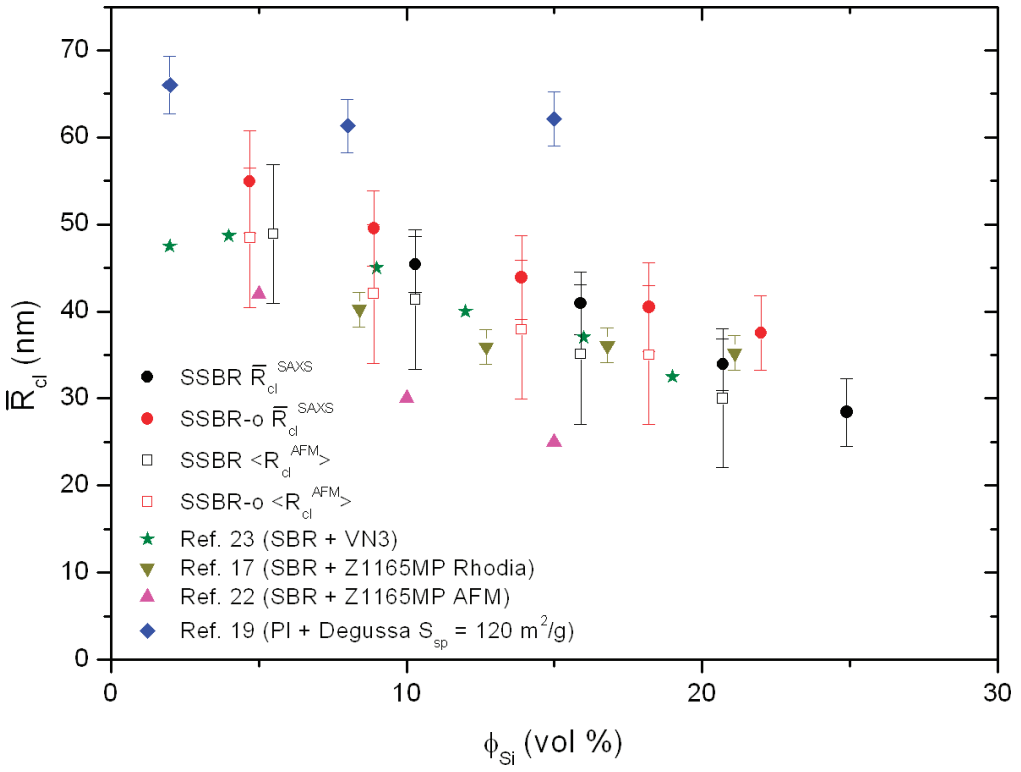

FIG. 9. — Comparison of cluster radii from MBM and AFM analysis results, with reported results on similar systems.

higher for the oil extended compounds. We can conclude that although AFM and SAXS are completely independent approaches, the obtained $\overline{R_{cl}^{SAXS}}$ and $\langle R_{cl}^{AFM} \rangle$ values are in close agreement within the experimental uncertainties. The visible tendency to observe slightly lower radii in AFM than in SAXS may be explained by the fact that the fitted $\overline{R_{cl}^{SAXS}}$ are a measure derived from higher orders of the cluster sizes, if these are not monodispersed.

Cluster Structure in Comparison with Literature Results. In Figure 9, the results from the cluster structure are compared to data from the literature. As an example, the average cluster radius is plotted together with the findings from Baeza et al.,[23] Schaefer et al.,[17] and Schneider et al.[22] for similar silica-filled rubbers, that is, SBR-based rubbers. The microstructures of the used SBRs are rather different between all literature sources as well as the silica particles are from different suppliers. However, for consistency, only silica fillers with the same specific surface area (S_{sp} = 165 m^2/g) are considered here. Despite these differences, the cluster sizes derived in this work are in close agreement with the results from literature. The same trend is observed for the number of particles within a cluster (data not shown). This may lead to the conclusion that the silica itself determines the resulting cluster structures, irrespective of the SBR microstructure. Nevertheless, significantly higher cluster sizes are observed for similar silica dispersed in a polymer of different type.[19] Moreover, Mihara et al.[21] demonstrate that the silica specific surface area affects the final cluster and agglomerates sizes, but that the SBR composition and mixing parameters are also important.

Evaluation of the Modified Beaucage Model. Figure 10 shows the scattering diagram for a 50 phr S-SBR compound. These experimental results (□) were fitted by using the Beaucage (see Beaucage Analysis) model as well as the MBM (see MBM Analysis). Taking only the overall fitting

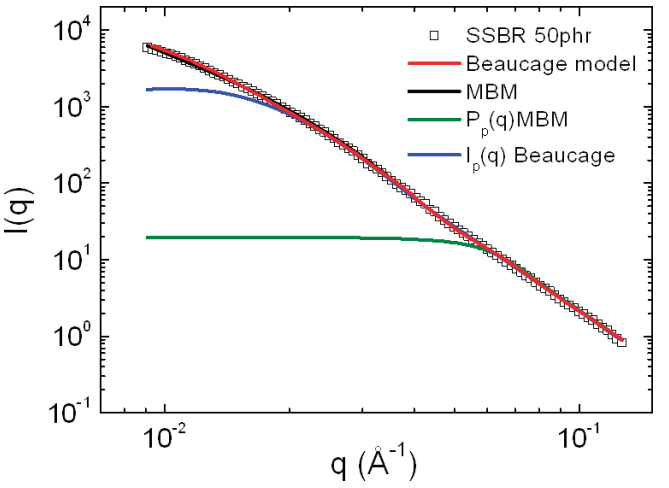

FIG. 10. — Scattering diagram for a 50 phr S-SBR compound fitted by using Beaucage and MBM models.

quality into account, both models give an accurate description of the experimental data. However, a more detailed analysis shows severe differences between both. In Figure 10, a comparison of the modeled scattering contributions from the particle only is plotted. There, one can clearly see that the particle scattering of unmodified Beaucage model dominates in the complete observed q range (blue line). Therefore, the influence of the fit parameters related to the clusters is underestimated, which should dominate massively below $q \sim 0.025$ Å^{-1} (see Beaucage Analysis). As a result, the obtained values for H_3, H_4, d_{cl}, and $\overline{R_{cl}^{SAXS}}$ are very dependent on the initial guess and not unique. This dominating scattering of the clusters is much more reassembled by the MBM, leading to a more stable fitting procedure.

Table 6 shows the corresponding MBM fitting results, where cluster radii of ~41 nm can be observed. As shown in Table 4, cluster radii of ~28 nm are obtained from the Beaucage model for the same experiment. From section AFM, it is clear that the AFM-based approach clearly supports the observed MBM values over their Beaucage counterparts.

CONCLUSIONS

The hierarchical structure of the filler network in two different styrene–butadiene filled rubbers was studied by means of SAXS and AFM. S-SBR compounds with different silica contents were analyzed in comparison with their oil extended counterparts (S-SBR-o). SAXS scattering results were analyzed by using two different approaches: the commonly used Beaucage model and herein a modified version of the later, denoted as MBM. In addition, AFM studies were independently conducted. For those filler levels, where both techniques could be applied, cluster and particle sizes are in close agreement, supporting the approach proposed. The results reveal smaller cluster sizes for higher silica contents, in close agreement with literature data for similar systems. In particular, a more compact cluster structure was found by MBM in the oil extended compounds studied here. The present study has shown that the synergetic application of SAXS and AFM allows for consistent robust characterization of primary particles and clusters in terms of size and structure. As one next step, we intend to run SAXS/ultra-SAXS experiments at a high-brilliance synchrotron facility to extend the characterization toward the scale of filler networks and agglomerates. This would lead to the capability to address all relevant length scales of filler structures beginning from the primary particle up to the agglomerate level in a single experiment.

ACKNOWLEDGEMENTS

The authors gratefully acknowledge the support of the Spanish Ministry of Education (MAT2012-31088), Basque Government (IT-436-07), and Luxembourgish Fonds National de la Recherche. Financial support from European Union–funded "European soft matter infrastructure" (reference 262348 ESMI) is also acknowledged. The continuous outstanding collaboration and support by F. Petry and R. Mruk (Goodyear Innovation Center Luxembourg) are also greatly acknowledged. We also thank the Goodyear Tire & Rubber Company for the permission to publish this paper.

REFERENCES

[1]M.-J. Wang, RUBBER CHEM. TECHNOL. **71**, 520 (1998).

[2]M.-J. Wang, RUBBER CHEM. TECHNOL. **72**, 430 (1999).

[3]D. W. Schaefer, T. Rieker, M. Agamalian, J. S. Lin, D. Fischer, S. Sukumaran, C. Chen, G. Beaucage, C. Herd, and J. Ivie, *J. Appl. Crystallogr*. **33**, 587 (2000).

[4]G. Heinrich and M. Klüppel, *Filled Elastomers Drug Delivery Systems*, Springer, Berlin, 2002, Vol. 160.

[5]S. Cerveny, R. Bergman, G. A. Schwartz, and P. Jacobsson, *Macromolecules* **35**, 4337 (2002).

[6]M. Klüppel, *Filler-Reinforced Elastomers/Sanning Force Microscopy*, Springer, Berlin, 2003, Vol. 164.

[7]S. Cerveny, G. A. Schwartz, J. Otegui, J. Colmenero, J. Loichen, and S. Westermann, *J. Phys. Chem. C* **116**, 24340 (2012).

[8]C. G. Robertson and C. M. Roland, RUBBER CHEM. TECHNOL. **81**, 506 (2008).

[9]J. G. Meier, J. Fritzsche, L. Guy, Y. Bomal, and M. Klüppel, *Macromolecules* **42**, 2127 (2009).

[10]J. Otegui, G. A. Schwartz, S. Cerveny, J. Colmenero, J. Loichen, and S. Westermann, *Macromolecules* **46**, 2407 (2013).

[11]M. M. Kummali, L. A. Miccio, G. A. Schwartz, A. Alegría, J. Colmenero, J. Otegui, A. Petzold, and S. Westermann, *Polymer* **54**, 4980 (2013).

[12]D. J. Kohls and G. Beaucage, *Curr. Opin. Solid State Mater. Sci*. **6**, 183 (2002).

[13]F. Ehrburger-Dolle, M. Hindermann-Bischoff, F. Livet, F. Bley, C. Rochas, and E. Geissler, *Langmuir* **17**, 329 (2000).

[14]A. V. Teixeira, I. Morfin, F. Ehrburger-Dolle, C. Rochas, P. Panine, P. Licinio, and E. Geissler, *Compos. Sci. Technol*. **63**, 1105 (2003).

[15]J. Ramier, C. Gauthier, L. Chazeau, L. Stelandre, and L. Guy, *J. Polym. Sci. B Polym. Phys*. **45**, 286 (2007).

[16]P. Mélé, S. Marceau, D. Brown, Y. de Puydt, and N. D. Albérola, *Polymer* **43**, 5577 (2002).

[17]D. W. Schaefer, C. Suryawanshi, P. Pakdel, J. Ilavsky, and P. R. Jemian, *Physica A* **314**, 686 (2002).

[18]G. A. Schwartz, S. Cerveny, Á. J. Marzocca, M. Gerspacher, and L. Nikiel, *Polymer* **44**, 7229 (2003).

[19]A. Botti, W. Pyckhout-Hintzen, D. Richter, V. Urban, E. Straube, and J. Kohlbrecher, *Polymer* **44**, 7505 (2003).

[20]L. Conzatti, G. Costa, M. Castellano, A. Turturro, F. M. Negroni, and J. F. Gérard, *Macromol. Mater. Eng*. **293**, 178 (2008).

[21]S. Mihara, R. N. Datta, and J. W. M. Noordermeer, RUBBER CHEM. TECHNOL. **82**, 524 (2009).

[22]G. J. Schneider, V. Vollnhals, K. Brandt, S. V. Roth, and D. Göritz, *J. Chem. Phys*. **133**, (2010).

[23]G. P. Baeza, A.-C. Genix, C. Degrandcourt, L. Petitjean, J. Gummel, M. Couty, and J. Oberdisse, *Macromolecules* **46**, 317 (2012).

[24]A. Banc, A.-C. Genix, M. Chirat, C. Dupas, S. Caillol, M. Sztucki, and J. Oberdisse, *Macromolecules* **47**, 3219 (2014).

[25]G. Beaucage, *J. Appl. Crystallogr*. **28**, 717 (1995).

[26]G. Beaucage, *J. Appl. Crystallogr*. **29**, 134 (1996).

[27]H. Boukari, J. S. Lin, and M. T. Harris, *J. Colloid Interface Sci*. **194**, 311 (1997).

[28]*Fractals and Disordered Systems*, A. Bunde and S. Havlin, Eds., Springer-Verlag, New York, 1991.

[29]A. Hasmy, R. Vacher, and R. Jullien, *Phys. Rev. B* **50**, 1305 (1994).

[30]G. Beaucage, H. K. Kammler, and S. E. Pratsinis, *J. Appl. Crystallogr*. **37**, 523 (2004).

[31]B. H. Zimm, *J. Chem. Phys*. **14**, 164 (1946).

[32]B. Hammouda, *Polym. Rev*. **50**, 14 (2010).

[33]O. Sahin, *Rev. Sci. Instrum*. **78**, 103707 (2007).

[34]O. Sahin, S. Magonov, C. Su, C. F. Quate, and O. Solgaard, *Nat. Nanotechnol*. **2**, 507 (2007).

[35]O. Sahin and N. Erina, *Nanotechnology* **19**, 445717 (2008).

[36]I. Horcas, R. Fernandez, J. M. Gomez-Rodriguez, J. Colchero, J. Gomez-Herrero, and A. M. Baro, *Rev. Sci. Instrum*. **78**, 013705 (2007).

[37]C. Oh and C. M. Sorensen, *Curr. Opin. Colloid Interface Sci*. **193**, 17 (1997).

[38]K. Nusser, S. Neueder, G. J. Schneider, M. Meyer, W. Pyckhout-Hintzen, L. Willner, A. Radulescu, and D. Richter, *Macromolecules* **43**, 9837 (2010).

[*Received February 2015, Revised August 2015*]

APPENDIX

REAL AND APPARENT RADIUS

Before performing any statistical AFM-based analysis, it is worth stressing the differences between the structure of the "real" material and the observed filler structure in a "material sample." As AFM samples are prepared by cutting the real material into thin sheets, and images contain information of the surface, there is a distortion in the observed cluster and aggregate sizes.

Figure A1 shows a scheme of the observed sizes when obtained from a plane (A-A′ in this example) by using AFM. For a given cluster of (real) radius R, the probability of observing an apparent radius R_i depends on the position of this cluster with respect to the A-A′ cutting plane. By assuming a large enough number of these structures, every cutting plane becomes equally probable.

Therefore, the relationship between AFM observed radius and the real value is defined by the average, $\langle R_i \rangle = \int_0^R \frac{\sqrt{R^2 - r^2}}{R} dr$.

At this point, it is worth noticing that a cluster is not really "cut" during sample preparation, but somewhat "revealed" to different extents by ripping off the polymer above it. This means that there is always some polymer above silica structures affecting the observed size. The amount of "detected" polymer, in turn defining the measured apparent radius, also depends on the imaging parameters (such as indenting depth, among others). Figure A2 shows some typical cluster structures in a 15 phr S-SBR sample, as observed by soft and moderate tapping. As shown, a detectable layer of polymer can be observed in soft tapping images ($A_{sp}/A_0 < 0.1$) due to the low tip indenting depth. However, as the tapping strength is increased, the hard silica surface below this polymer layer is clearly revealed.

IMAGE FILTERING AND PARTICLE COUNTING

As already shown, AFM imaging parameters can be appropriately tuned to achieve a rather good contrast between silica structures and rubber. Therefore, a particle count analysis can be performed by phase filtering (or a filtering with any other available experimental channel, as dissipation or modulus, among others) these images to separate particles and aggregates from rubber. In a second step, filtered data can be further processed to obtain a particle count by equivalent disk radius of the observed structures. So, the obtained data are then plotted as histograms and fitted with two lognormal distributions representing a) particles and b) clusters of

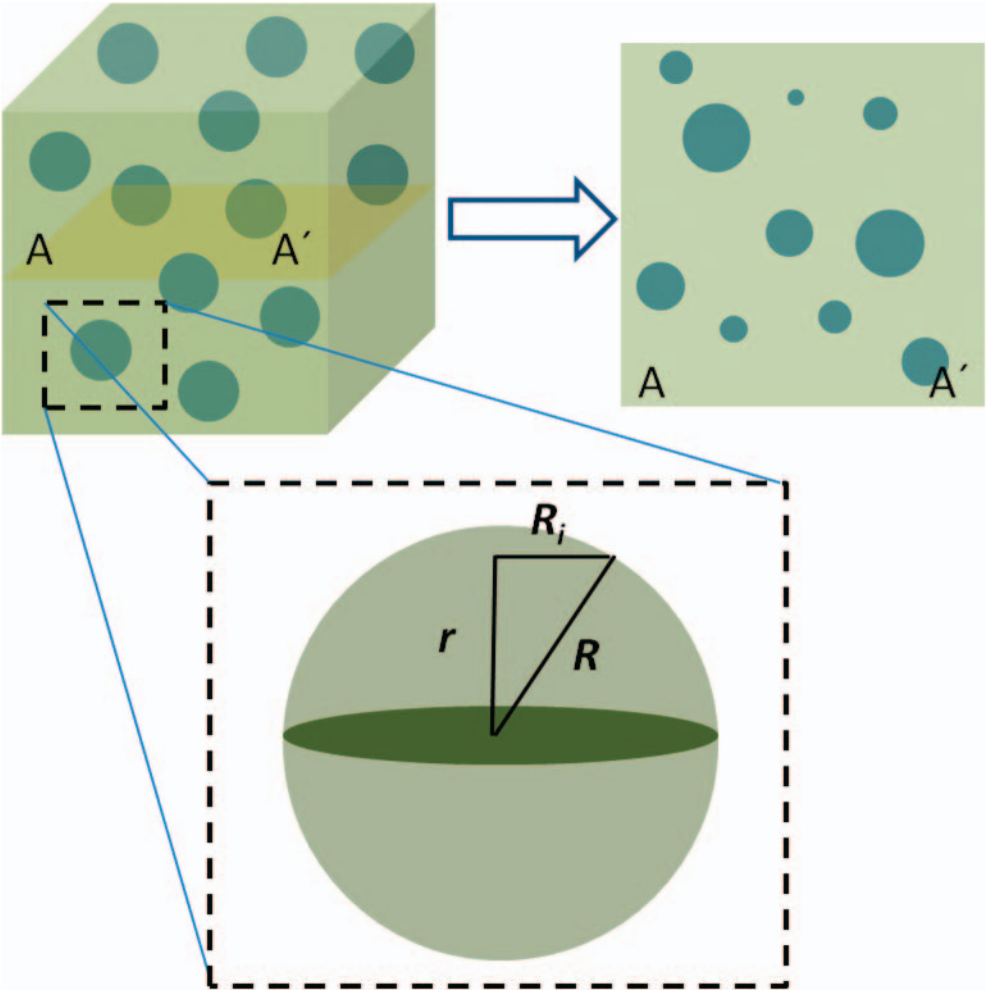

FIG. A1. — Scheme of real (R) and apparent radii (R_i) in AFM experiments.

particles. The apparent cluster average radius, $\langle R_{cl}^{AFM} \rangle$, is then obtained from Eq. A1 (first moment of Eq. 8), after applying the previously mentioned cutting effect correction ($\langle R \rangle = \frac{4}{\pi} \langle R_i \rangle$)

$$\langle R_{cl}^{AFM} \rangle = \langle R \rangle \exp\left(\frac{\sigma^2}{2}\right) \tag{A1}$$

In the case of particles, the corresponding parameters $\langle R \rangle$ and σ were fixed from previous SAXS fittings (because most of these structures are in the limit of the microscope resolution). Therefore, complementary cluster and agglomerate information can be obtained from standard AFM experiments. A representative image of the above-mentioned process is shown in Figure A3.

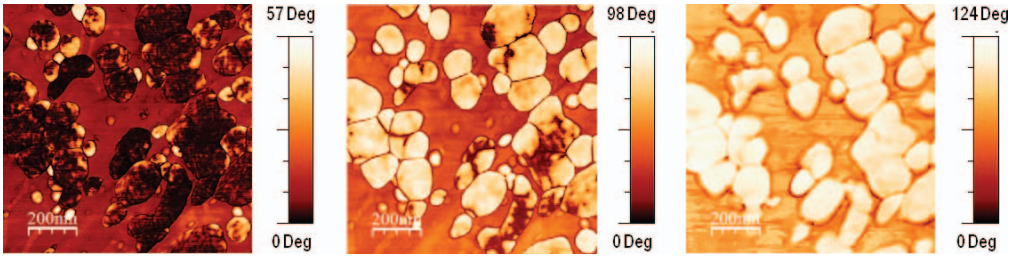

FIG. A2. — Mechanical phase images of the polymer above silica clusters in a 15 phr S-SBR sample. The experiments were performed by using (from left to right) soft to moderate tapping.

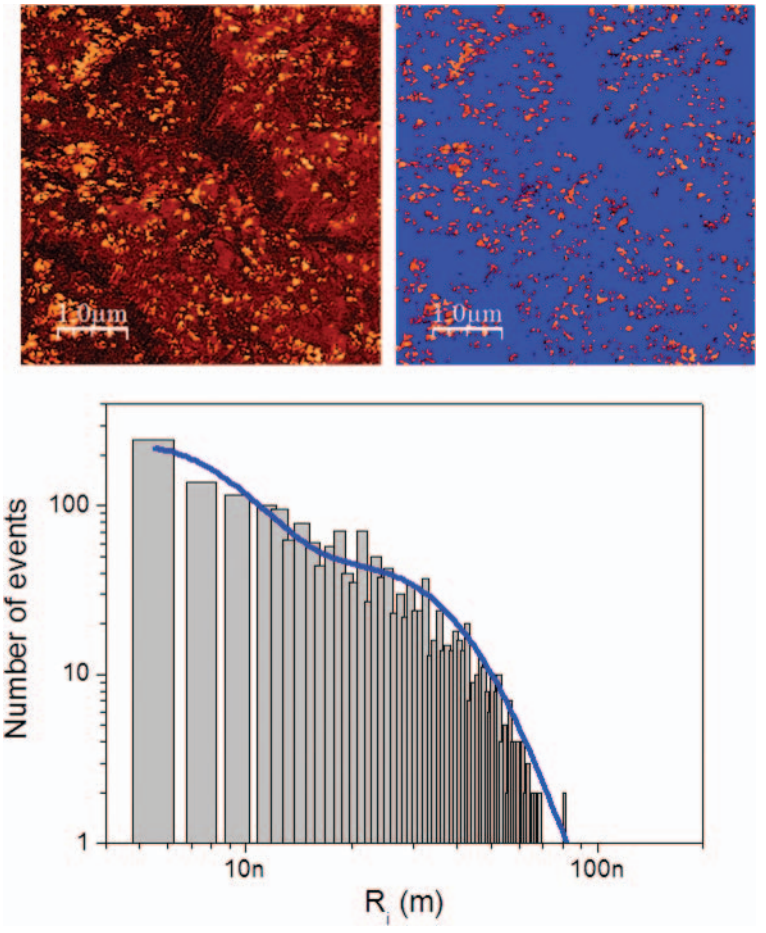

FIG. A3. — HMX peak force images of S-SBR-o 50 phr. The raw peak force image and the filtered result are presented. Resulting radius histogram is shown below, where blue line stands for the fitting results of lognormal distributions (representing particles and clusters).